Physics in Medicine & Biology

PAPER • OPEN ACCESS

Microdosimetry modeling with auger emitters in generalized cell geometry

To cite this article: Teresa L Palmer *et al* 2021 *Phys. Med. Biol.* **66** 115023

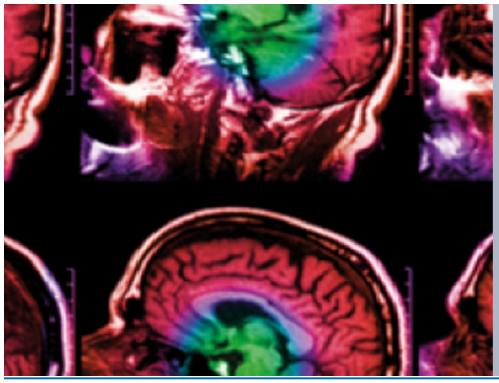

IOP Publishing Phys. Med. Biol. 66 (2021) 115023 https://doi.org/10.1088/1361-6560/ac01f5

Physics in Medicine & Biology

IPEM Institute of Physics and Engineering in Medicine

OPEN ACCESS

RECEIVED
19 December 2020

REVISED
11 May 2021

ACCEPTED FOR PUBLICATION
17 May 2021

PUBLISHED
3 June 2021

PAPER

Microdosimetry modeling with auger emitters in generalized cell geometry

Teresa L Palmer[1], **Kinga Tkacz-Stachowska, Roar Skartlien, Nasrin Omar, Sindre Hassfjell, Andreas Mjøs, Johannes Bergvoll, Ellen M Brevik and Olaug Hjelstuen**

Institute for Energy Technology (IFE), PO Box 40, NO-2027 Kjeller, Norway

[1] Present address: Venabo Analytics, Fetsund, Norway.

E-mail: teresa.palmer@venabo.no

Keywords: microdosimetry computer modeling; local radioimmunotherapy; targeted radiation therapy; auger emitters

Abstract

A microdosimetry model was developed for the prediction of cell viability for irregular non-spherical cells that were irradiated by low energy, short range auger electrons. Measured cell survival rates for LNCaP prostate cancer were compared to the computational results for the radioisotopes ^{177}Lu and ^{161}Tb (conjugated to PSMA). The cell geometries used for the computations were derived directly from the cell culture images. A general computational approach was developed to handle arbitrary cell geometries, based on distance probability distribution functions (PDFs) derived from basic image processing. The radiation calculations were done per coarse grained PDF bin to reduce computation time, rather than on a pixel/voxel basis. The radiation dose point kernels over the full electron spectrum were derived using Monte Carlo simulations for energies below 50 eV to account for the propagation of auger electrons over length scales at and below a cellular radius. The relative importance of short range auger electrons were evaluated between the two nuclide types. The microdosimetry results were consistent with the cell viability measurements, and it was found that ^{161}Tb was more efficient than ^{177}Lu primarily due to the short range auger electrons. We foresee that imaging based microdosimetry can be used to evaluate the relative therapeutic effect between various nuclide candidates.

1. Introduction

The dose distribution in radioimmunotherapy can be controlled by a selection of carrier molecules that have affinity to specific cancer cell receptors (antibodies or affibodies), and by choosing specific radionuclides with a characteristic penetration depth of the emitted particles (electrons or alpha particles). Various radionuclides can be used with the same targeting molecule, and the selection of the optimal radionuclide may depend on the size and type of the tumor, and the particular antibody internalization fraction between the cell membrane and the cell interior (Cornelissen and Vallis 2010). *In vitro* studies are normally used to determine the cancer cell survival rate when the cells are exposed to a certain radiolabelled targeting molecule (Steffen *et al* 2008, Marcatili *et al* 2016). To complement and plan such experiments, one could use microdosimetry calculations to estimate the relative biological effect (RBE) of different nuclides. With new possibilities of more advanced computer based microdosimetry, we expect that in-silico computations will be used as a screening tool for use prior to *in vitro* testing.

The use of radionuclides that emit short range auger and conversion electrons appear to have substantial advantages in terms of reducing the radiation damage outside the tumor (Hindie *et al* 2016), and to increase the biological effect (Müller *et al* 2014). In the current work we will be concerned with computational microdosimetry tailored to *in vitro* testing of new auger electron based radioimmunotherapies. The computations represent primarily an implementation of accurate physical models for the radiation field in the cellular and sub-cellular environments. The cell viability can then be estimated from the calculated radiation

field that is available to the DNA. Our computations are tailored to handle the non-spherical cell geometry as measured, and this is needed for accurate testing of auger-based radioimmunotherapies.

The maximum range of propagation of auger electrons from the radionuclide is below 10 μm (Cornelissen and Vallis 2010), and a cell radius is of similar order. It is therefore clear that the location of the radionuclide in the cell is of great importance for the radiation intensity variation in the cell interior and for the radiation intensity at the location of the DNA. A particularly important geometrical effect is that an irregularly shaped cell membrane (as opposed to a perfect sphere or ellipsoid) directly modulates the radiation intensity in the cell nucleus, and large differences in the absorbed dose to the nucleus can be found between irregular and spherical cell models (Sefl *et al* 2015). Using a spherical model for non-spherical cell types can then lead to errors in the dose (Falzone *et al* 2015, Maria *et al* 2018). Furthermore, dose calculations using a sample of identical cell sizes rather than a distribution of sizes can give large errors in the dose estimate as well (Oliver and Thomson 2018).

3D imaging is necessary to fully capture the cell membrane shape, as well as the nucleus shape, size and location. The use of state-of-the-art imaging techniques based on 3D laser scanning microscopy and super-resolution microscopy of immunofluorescent stained specimens can be used (Steffen *et al* 2008) for this purpose. The challenge with 2D imaging (in terms of a projection of the cell structure to the image plane) is to formulate mathematical models to represent the actual 3D geometry, based on knowledge about cell structure. A quasi 3D approach is to use image projections along all three axes with or without fluorescent staining, and construct a 3D cell model from these projections. Cell geometry in tumors would be needed for *in vivo* applications, and we foresee modeling of these 3D cell cluster geometries based on more advanced mapping techniques such as tumor sectioning and 3D imaging with staining.

Once the accumulated dose to the cell nuclei has been calculated from a microdosimetry model, one can evaluate the cell survival probabilities. We use the linear quadratic (LQ) model which incorporates the accumulated dose in the cell nucleus and predicts the associated cell survival probability.

The main goal with the current work was to evaluate whether microdosimetry is a suitable evaluation tool for estimating the difference in cell viability between different radionuclides, given the same targeting molecule. Special focus was given on the effect of cell geometry. ^{177}Lu and ^{161}Tb radionuclides were conjugated to PSMA for the treatment of LNCaP prostate cancer. Cell geometry data from the *in vitro* cell cultures were used directly in the microdosimetry calculations.

2. Microdosimetry for general cell geometries

2.1. Overview of the dosimetry calculations

It is generally accepted that the most relevant quantity for calculating cell survival probability is the energy deposition in the cell nucleus that is available for DNA bond breaking, although cell membrane mediated effects due to irradiation of the cell membrane and the surrounding medium may also be an important additional mechanism (Paillas *et al* 2016). The total dose to the cell nucleus includes the self dose plus the cross dose due to radiation from neighboring cells. The self dose is the most important contribution for the short range auger electrons, while beta-electrons propagate over longer distances. The latter can give a significant cross dose contribution, in particular for multi-layered cell structures and 3D cell clusters and tumors.

Radiation from the cell membrane and the interior cytoplasm may both contribute to the irradiation of the DNA, depending on the internalization ratio of the given targeting molecule. Auger emitters are generally more effective when bound to carrier molecules that are transported through the cell membrane into the cytoplasm so that the DNA-carrying nucleus can be reached within a typical propagation range of a few microns.

The model generates a population of cells with a distribution of sizes and shapes. Applied activity is then assigned to each cell, distributed in the cell membrane and the cytoplasm. We assumed that the radioactivity was distributed uniformly on the cell membrane and in the cytoplasm volume. This represents an average state when the radioactivity associated to the endosomes can move without much restriction in the cytoplasm volume.

The dose to each cell nucleus is then calculated. The probability of cell death based on the LQ model is calculated and a survival fraction of the sample over time is generated. In general terms, the absorbed dose to a target region T (in our case, the cell nucleus) can be expressed as the sum of the contribution from all source regions $\mathcal{S}$ (e.g. cytoplasm and cell membrane), both in the target cell and in neighboring cells

$$D(T) = \sum_{S} A(\mathcal{S}) S(T \leftarrow \mathcal{S}), \tag{1}$$

where A is the activity in the source region, the accumulated energy or dose deposited per mass is $D = E/m$ in units of gray and the S value is the absorbed dose in the target per disintegration in the source. The S value is the sum of energy deposited for each radiation mode

$$S(T \leftarrow \mathcal{S}) = \sum_k \frac{\Delta_k \phi_k (T \leftarrow \mathcal{S})}{m_T}, \tag{2}$$

where Δ_k is the energy in the radiation mode k, ϕ_k is the fraction of energy emitted in $\mathcal{S}$ that is absorbed in the target T, and m_T is the mass of the target. We calculated the S values by using Monte Carlo simulations in the given cell geometry.

The target region for calculating the dose to the cell is the nucleus, and the source region is in general the cell nucleus, cell membrane and the cytoplasm in the same cell (self dose) and in neighboring cells (cross dose). For these cell experiments, PSMA internalizes into the cell membrane and the cytoplasm. Our dosimetry model took into account sources in the cell membrane and the cytoplasm. The total self dose to a single cell nucleus can then be expressed as

$$D(N) = A(Cy)S(N \leftarrow Cy) + A(M)S(N \leftarrow M). \tag{3}$$

2.2. PDF approach for generalized cell geometries

For auger electrons, the S values will strongly depend on the cell size and geometry, and treating the cells as spheres or ellipsoids will lead to errors in the S values. We use a method that allows us to calculate the dose to the cell nucleus for arbitrary non-spherical cell geometry. If one considers the distances between all voxel-pairs in a 3D volume over a cell, there will be a large number of pairs with nearly the same separation distance, and the associated radiation kernels are nearly the same. These redundant calculations are eliminated by using a histogram for the voxel separations, and the radiation kernel is applied only once per histogram bin. This approach reduces the computational time by a factor of the order of 100.

To illustrate this approach, consider the S value for the self dose to the nucleus from activity on the cell membrane. The S value is a surface integral over the cell membrane or cell surface

$$S(N \leftarrow M) = A_{\mathrm{m}} \int_{\text{cell surface}} d\Omega \int_{\text{nucleus}} d^3\mathbf{r}' K(|\mathbf{r} - \mathbf{r}'|), \tag{4}$$

where Ω is the solid angle, and $\mathbf{r}$ is the distance vector from the nucleus center to the surface, and K is the dose point kernel that is evaluated by Monte Carlo simulation for any nuclide and medium. This kernel includes all the particle physics involved with the propagation of the electron and the interaction with the background medium and has units energy/volume/activity.

The calculation for the S value of the contribution of activity from the cytoplasm to the target in the nucleus, $S(N \leftarrow CY)$ is similar, with the integral over the surface of the cell replaced by an integral over the cell volume.

In the probability distribution function (PDF) approach, the integral over angle is replaced by a sum over the histogram bins of the distances between the cell membrane and the nucleus center, termed the 'distance probability distribution function' (distance PDF)

$$S(N \leftarrow M) = A_{\mathrm{m}} \sum_{i=1}^{n} p_{\mathrm{m}}(r_i) \int_{\text{nucleus}} d^3\mathbf{r}' K(|\mathbf{r}_i - \mathbf{r}'|), \tag{5}$$

where p_{m} is the distance PDF, and r_i is the center value in bin i. There must be a sufficient number n of bins to resolve the structure of the PDF, but n should be small enough to save computational time relative to a direct voxel based approach for the surface integral. There is one PDF for every cell in order to calculate cell-by-cell survival rates.

The kernels K were evaluated for a limited number of pre-determined radii r_j (typically 100 points) a non-uniform grid using dense sampling where the kernel gradients are large. The kernels were also integrated over electron energy. The kernel value $K(r)$ for any required r was evaluated using fast linear interpolation in the lookup-table $K(r_j)$. Image samples from cell cultures and a geometrical cell model (discussed later) were used to generate the distance PDFs, after the individual cells were identified by image processing (discussed later).

2.3. Monte Carlo simulations tailored for low energy auger electrons

The energy spectra of ^{177}Lu and ^{161}Tb including auger electrons were taken from the ENSDF database (ENSDF 2019) and the dose point kernels were used to calculate the dose by spatial integration over the local cell (self dose), and neighboring cells (cross dose). The accumulated dose to the cell nuclei were integrated over time using the cell geometry statistics and a realization of an ensemble of log-normally distributed activities A_{cell} over all cells. To calculate the dose point kernels $K(r)$ we use GEANT4 to calculate the lower energy auger electrons. A uniform nucleus and cytoplasm medium of water was assumed.

2.4. The cell survival probability model

To estimate the cell survival probability for a given dose to the nucleus, we use the standard LQ model (van Leeuwen *et al* 2018), although its validity is debated (Hanin and Zaider 2010). The probability of cell death as a function of cumulated dose D is given by

$$P = e^{-\alpha D - \beta D^2}. \quad (6)$$

The factor α is the probability of lethal damage to the cell per unit absorbed dose and parametrizes the damage caused by a single particle track. The factor β is the probability of lethal damage per unit dose squared and represents lethal damage caused by two separate particle tracks.

The primary radiation mode from an isotope influences the cell survival probability through the α and β parameters, and they are a function of the energy distribution (energy spectrum) of the radiation and the particle track density. Furthermore, they are also dependent on the cell type in question via DNA geometry in the nucleus and the efficiency of DNA repair mechanisms. The ^{161}Tb and ^{177}Lu isotopes both emit beta-particles of similar energy ranges, and therefore we expect that the α and β parameters should be of comparable magnitude for a given cell type.

We did not find established α and β parameters for ^{161}Tb and ^{177}Lu in combination with prostate cancer *in vitro* studies. However, Pedicini *et al* (2013) reviewed data of a total of 2634 patients that underwent ionizing radiation treatment for prostate cancer and found the average values $\alpha = 0.16$ and $\beta = 0.054$, consistent with other datasets (van Leeuwen *et al* 2018). We use these values for both nuclides. The comparison to the experimental data values for cell survival probabilities for both ^{161}Tb and ^{177}Lu were reasonable with these parameters. Consequences for a possible difference between the parameters for the two nuclides are discussed further below. According to Valentin (2003) the RBE values can be regarded as 1.0 for auger emitters located in the cell membrane and cytoplasm and 4.0 for nuclides located in the cell nucleus. We therefore used the same RBE of 1.0 for both ^{161}Tb and ^{177}Lu.

The cumulated dose for each cell n over time and the cell survival probability function are then used to label each cell as living or dead. This gives the surviving fraction N_{alive}/N of an ensemble N of cells that have been exposed to the same cumulated dose D.

2.5. An overview of the microdosimetry calculation

The primary input data is the cell geometry statistics in terms of cell positions in the image plane, and the associated distance PDF's for each cell. The input parameters are isotope type, internalization fraction of targeting constructs and the average applied activity per cell. The main output of the microdosimetry program is the accumulated dose in the cell nuclei, and the average cell survival probability for an applied activity. In this work, a specified activity of either ^{177}Lu or ^{161}Tb was applied to the ensemble of cells, using a log-normal distribution.

For comparison to the cell line experiments, the calculated dose to each cell nucleus was integrated over a time and the cell survival probability was calculated using the LQ model. The dose to every cell nucleus was calculated using Monte Carlo derived kernel functions, one for each PDF bin. The average cell survival probability was calculated using a number of values of applied activity.

An ensemble of 10 000 cells with a log-normal distribution of mean cell radii was generated and the mean and standard deviation of this distribution was set equal to that of the measured average radii from the cell images. A larger ensemble of cells were used in the calculations than the number of cells extracted from the images, primarily to obtain better statistics over a wide range of cellular dose values.

Each radius in the log-normal distribution bin was assigned to one distance PDF group by choosing the nearest neighbor radius to that of the corresponding distance PDF average radius. The cell geometry model (section 4) was then implemented for each of the distance PDF groups in order to calculate the self-doses. The left hand panel in figure 1 shows the log-normally distributed cell radii. The distance PDF of the measured cells were organized in about 20 groups of increasing mean cell radius.

The activity was assigned randomly to each cell using a log-normal distribution, without specifying the surface area distribution (following earlier microdosimetry work e.g. MIRDCell). The log-normal distribution takes the mean value as the total activity taken up by the cells (2% of the applied activity) divided by the number of cells. The internalization into the cell membrane and the cytoplasm was assumed to be the same for each cell. The internalization rate of PSMA in LnCAP cells is 60%. We assigned 40% of the activity for each cell to the membrane and 60% distributed uniformly throughout the cytoplasm.

The middle panel in figure 1 shows the activity distribution over all cells. We did not incorporate possible cell growth and cell death effects on the activity distribution. The right-hand panel figure 1 shows an example of the distribution of the calculated cumulated dose to the cell nuclei after 5 d. There is a large span of dose values due to several factors; the activity variation over the cells, the spatial distribution of cells in the image plane that affects the cross dose, and the varying cell geometry that affects the self dose.

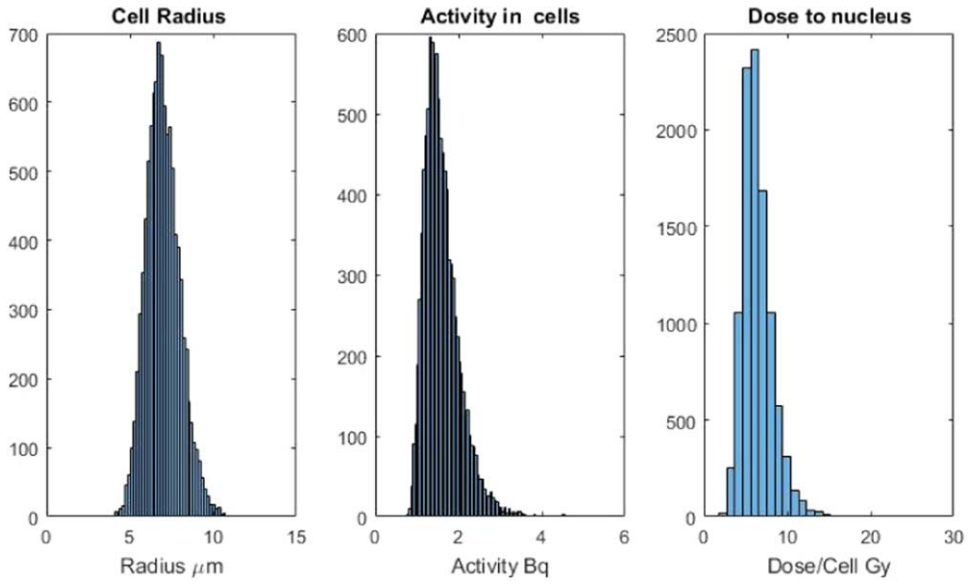

Figure 1. Average cell radius distribution (left), log-normally distributed activity over the cells (middle), and cumulated dose distribution over the cells after 5 d.

3. Cell line experiments

3.1. Preparation of ^{177}Lu-PSMA-617 and ^{161}Tb-PSMA-617

PSMA-617 (ABX, Germany) was radiolabeled either with ^{177}Lu (ITG, Germany) or ^{161}Tb. The latter was produced at the IFE research reactor JEEP II, with purification through a modified Lehenberger method (Lehenberger *et al* 2011). The radiochemical purity (RCP) was determined by instant thin-layer chromatography (iTLC) with a 0.1 M citrate buffer as the mobile phase. The stability of cold PSMA-617 was analyzed both in DMSO and 0.4 M NaOAc-buffer in different temperatures. The stability of ^{177}Lu-PSMA-617 and ^{161}Tb-PSMA-617 was determined over time, with RCP as an indication of stability.

3.2. ABC analysis

The ability of the constructs to bind to PSMA-receptors was analyzed by using the antigen binding capacity (ABC) method, by incubating an increasing number of LNCaP cells with the targeting constructs and analyzing the amount that attached to the cells. The maximum ABC was found to be 97% for ^{177}Lu-PSMA-617 and 93% for ^{161}Tb-PSMA-617, confirming that the constructs are effective.

The ABC was calculated by using the Lindmo method (Lindmo and Bunn 1986). A linear fit to the inverse of ABC as function of the inverse of the number of LNCaP cells is performed, and the intersection of the fitted line with the y-axis indicates 1/ABC at infinite number of receptors or cells.

3.3. Cell culture

LNCaP are AR-positive hormone responsive prostate cancer cells (ATCC, USA). They were cultured in a RPMI-1640 medium supplemented with 10% fetal bovine serum and 1% penicillin streptomycin at 37 °C in a humidified atmosphere with 5% CO_2. The cells were cultured in T75 and T125 flasks (Thermo Fisher Scientific) and were observed daily in a microscope. The medium was changed once or twice a week depending on the cell confluence. The cells grew in a monolayer with a population of semi-attached cells, and they were seeded on 96-well plate, 6-well plate, and 12-well plate (flat bottomed) depending on the cell size and growth rate. Live cells were counted with an automatic cell counter (Countess®, Invitrogen) in the presence of trypan blue to exclude dead cells.

The cells were first allowed to grow for 24 h while incubated at 37 °C in a humidified atmosphere with 5% CO_2. The radiolabeled antibodies were then added to interact with the cells from 4 to 6 h. The cells were then washed to remove radioactivity from the medium external to the cells, leaving only radioactivity on the cell membrane and in the cytoplasm. The cells were then incubated into the IncuCyte (Essen BioScience) instrument, to monitor the evolution of the cells over 4–5 d. We processed the images generated by this instrument to provide cell geometry data as input to the dosimetry calculations.

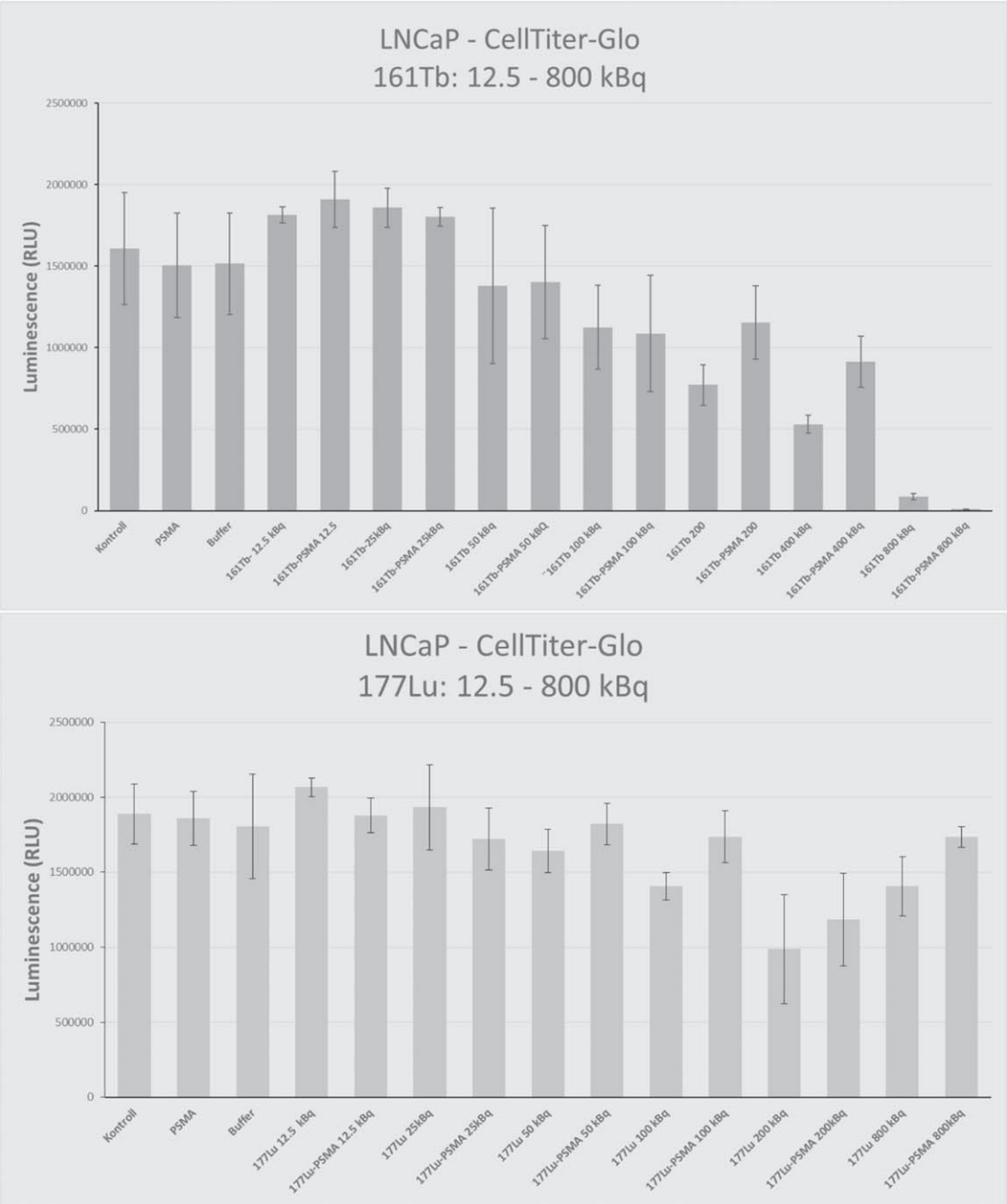

Figure 2. Example of results from the CellTiter-Glo® assay. The luminescence is proportional to the amount of ATP or the number of cells present in the well.

3.4. Luminescent cell viability assay

The CellTiter-Glo® approach utilizes bioluminescence to determine the number of viable cells in culture based on quantification of ATP (an indicator of metabolically active cells). The luminescent signal is catalyzed by a thermo-stable luciferase. The amount of ATP present in the cell culture is directly proportional to the number of cells present in culture (Crouch *et al* 1993).

The 96-well plates (in the IncuCyte) were at room temperature before the 50 μl medium was removed from each well, and 50 μl of CellTiter-Glo® reagent was added. The plates were mixed for approximately 2 min on a plate shaker to induce cell lysis. The cells were then incubated at room temperature for 10 min to stabilize the luminescent signal before the luminescence was recorded. The results of the cell assay are shown in figure 2.

3.5. Internalization and applied activity

The LNCaP cells were incubated with 12.5–800 kBq/well for both constructs, and each well had about 10 000 cells. For the dosimetry calculations, we assumed that the internalization ratio between the cell membrane and the cytoplasm is constant in time. This assumption is reasonable if the timescale for internalization is short

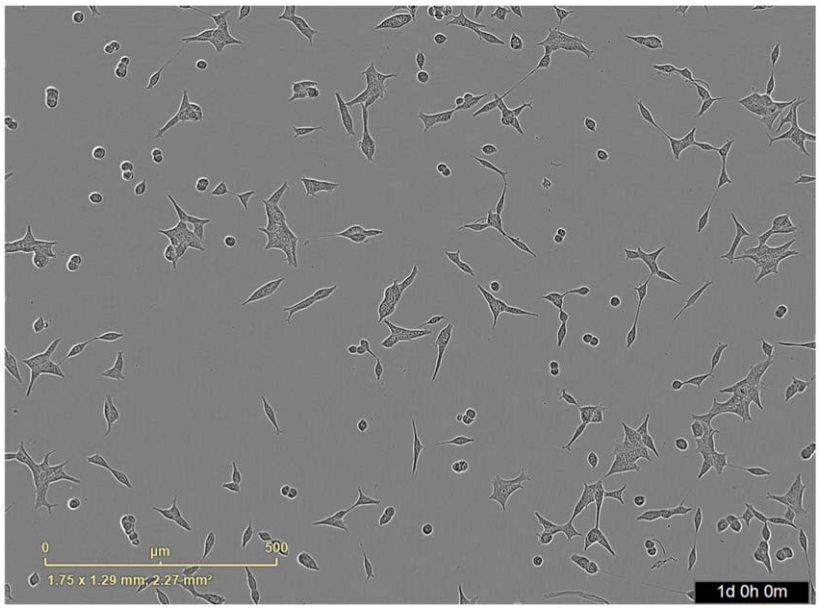

Figure 3. The figure shows a raw image from the IncuCyte instrument of untreated cell after 24 h of incubation. This represents the situation when radioactivity is added.

compared to the half-life of the isotopes. The uptake was estimated to be in the range 1%–5%, and this gives an initial average activity per cell in the range 0.0125–0.0625 Bq/cell for the lowest activity experiments and 0.8–4 Bq/cell for the highest applied activities. The internalized fraction of PSMA without mAB (monoclonal antibodies) reaches a maximum of 60% after 60 min, and with the presence of mAB the internalization reaches a maximum of 60% after 20 min, and the internalized fraction remains fairly constant for at least 6 h. The stability of labeled PSMA for a period over 6 h (data not shown) indicates that PSMA degradation during this period is minimal (Liu *et al* 1998). We assume that the internalization remains the same through the length of the experiment. The half-life of ^{177}Lu and ^{161}Tb is 6.7 and 6.9 d respectively, so that one can safely assume a constant internalization ratio over the half-life of both nuclides.

3.6. Time-lapse microscopy

Cellular growth and the effect of ^{177}Lu-PSMA-617 was observed in a visual microscope, and by time-lapse microscopy with the IncuCyte instrument. A camera placed inside the incubator allows live-cell imaging with a pre-determined frequency (e.g. every 3 h).

For the dosimetry, we used images of cells prior to adding radioactivity as shown in figure 3. It is the initial cell geometry that is the most relevant for the dosimetry calculations, since DNA bond breaking should occur within a timescale that is quite short compared to no the characteristic timescale of significant cell shape variation. After a few days, the radiation intensity has decayed and the cell geometry is more affected by metabolism and the shape changes of dead cells. For higher activities (up to 800 kBq/well in the current experiments), the DNA is damaged at earlier times, and the initial geometry is again the most relevant for the radiation calculations.

4. Image processing and geometry modeling based on 2D images

4.1. Image processing

Image processing routines were developed that scanned the cell images to generate a dataset of the distance histograms (or distance PDFs) for each cell. Figure 3 shows one of the images (1126 × 832 pixels) from the IncuCyte instrument. The images were filtered in terms of removing dead and deformed cells before image processing and extraction of the geometry data.

The cell membrane and cytoplasm regions in the images were extracted using standard morphological and region based image processing routines available in MATLAB. Figure 4 shows extracted perimeters of the cells, representing the outer rim of the cell membrane at the substrate.

Images with a total number of a few hundred cells, were used for developing the geometry statistics in the form of PDF's. The centroid (center of gravity) and equivalent diameter for each cell was stored, together with the distance PDF between the centroid and the cell membrane perimeter, and the distance PDF between the

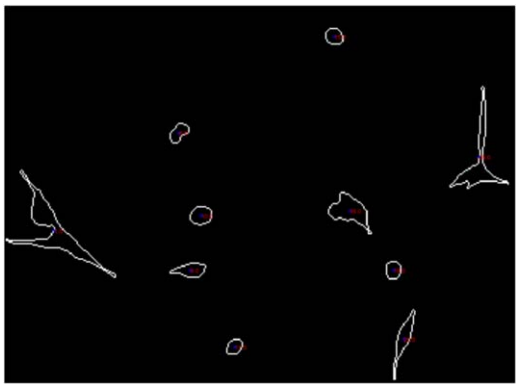

Figure 4. The figure shows a zoom-up of a processed image, with perimeters of the contact area between the cells and the substrate. These represent the outer rim of the cell membrane on the substrate. The corresponding centroids (assumed cell nuclei locations in the image plane) are marked with blue asterisks.

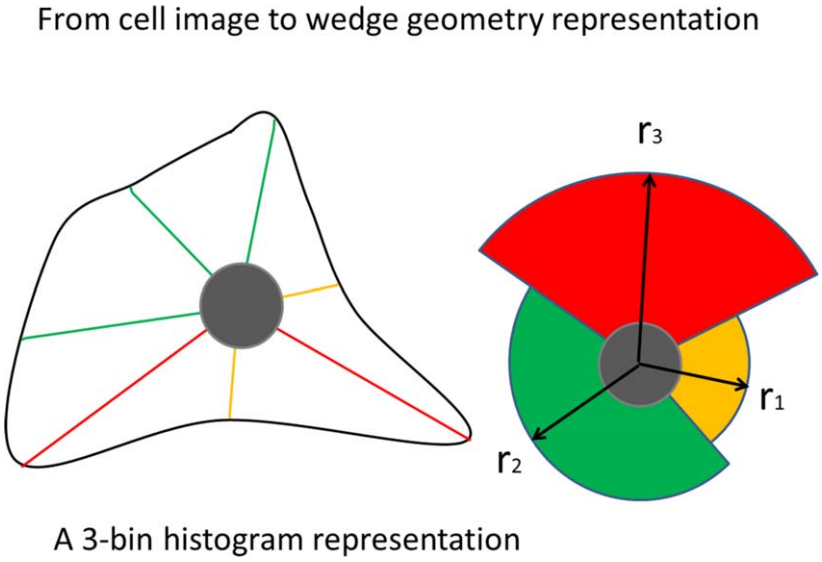

Figure 5. Perimeter histogram and wedge model. Left: the rim of a cell and the cell nucleus are shown, as well as a few radii that are color coded with small (yellow), medium (green) and large (red) radius, corresponding to a three-bin histogram. The corresponding three-wedge model of the cell is illustrated to the left, labeled with the respective bin values for the radii. The *angular* extension for each wedge corresponds to the number of measured radii that fall within each bin (the histogram value).

centroid and the imaged cell interior. We did not apply staining of the nuclei and we assumed that the cell nucleus is centered on the measured centroids.

4.2. Prostate cancer cell geometry modeling

The LNCaP cells display a large variety in shape when they evolve. The recorded images show that the smaller cells were approximately ellipsoidal and the larger cells had an irregular star-like geometry (figure 3).

Only 2D images of the cells were available, and a geometrical model was used to account for the structure in the third dimension, perpendicular to the image plane. The image plane usually coincides with the substrate on which the cells grow. For the geometry model for single cells, we adopted a 'wedged spherical cap model' as illustrated in figures 5 and 6.

A prostate cancer cell was represented by a number of wedges, one per PDF bin of a perimeter histogram $p_{\text{rim}}(r_i)$ as shown in figure 5. The perimeter distance is the separation between the cell center (centroid), and a point on the perimeter extracted from the image processing (figure 4). The perimeter length l_i or the angular extension of the wedge is proportional to the histogram value p_{rim} (number of occurrences for radius r_i).

The top membrane segment in each wedge is part of the spherical cap (part of a sphere cutoff by the substrate plane) as illustrated in figure 6. The main reason for choosing this geometry is the mathematical simplicity of the explicit formulae for the cytoplasm volume and top membrane area for each wedge. The surface and volume

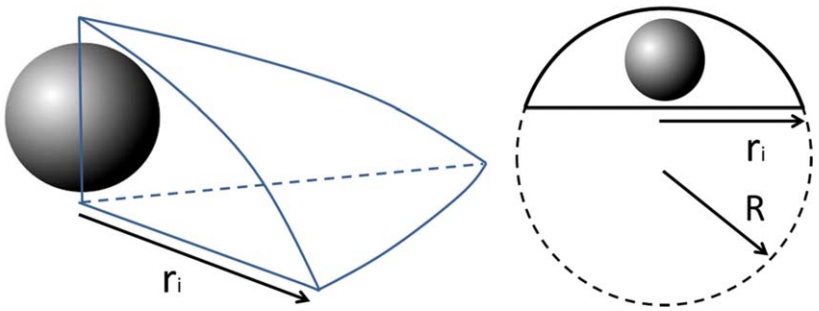

Figure 6. Geometry model for a single wedge. Left: each bin radius r_i for the perimeter histogram corresponds to a specific wedge representation. The bottom triangular segment coincides with the base area on the substrate. The cell nucleus is illustrated by the gray sphere. The curved triangular area at the top represents the cell membrane from the rim at the substrate, up to the corner (or apex) above the cell nucleus. The wedge is cut out from a spherical cap shown to the right. The radius R of the cut sphere is set by the requirement that the spherical cap should just encapsulate the cell nucleus with a given margin, and coincide with the radius r_i at the substrate.

integrals for the cell nuclear self dose can then also be expressed as a simple sum over wedge contributions, and each contribution is on explicit analytic form. This is much more efficient computationally, than integrating over a large number of voxel-pairs.

The perimeter length l_i, corresponding to the angular extension of the wedge, is approximately the fraction p_{rim} of the full circle with the corresponding radius r_i, namely $l_i = 2\pi p_{\mathrm{rim}}(r_i) r_i$.

The top membrane area for wedge i is

$$a_i = \pi(h^2 + r_i^2) p_{\mathrm{rim}}(r_i), \tag{7}$$

where the apex height of the wedge was chosen to be $h = 1.2R_{\mathrm{nucleus}}$, to encapsulate the cell nucleus with an added margin. The volume of the wedge is

$$V_i = \pi h(3r_i^2 + h^2) p_{\mathrm{rim}}(r_i)/6. \tag{8}$$

The total interior volume (nucleus and cytoplasm) and top surface area of a single cell is then $V_m = \sum_i V_i$ and $a_m = \sum_i a_i$ respectively. The nucleus was assumed to be spherical, and its radius was set to be slightly smaller than the minimum bin radius

$$R_{\mathrm{nucleus}} = 0.9\,\mathrm{Min}(r_i). \tag{9}$$

An integration over the cytoplasm volume and membrane surface for every wedge, and integration over the nucleus volume, is necessary.

The contribution to the self dose in the nucleus from each wedge volume and top membrane surface was obtained by analytic double integration over the nucleus volume and cytoplasm volume/top membrane (in the geometry shown in figure 6). The total dose was then obtained by summation over the wedge contributions. The calculated dose rate for the nucleus in cell n can be written

$$\dot{D}^n(\text{self dose}) = \sum_{r_i} A_{\mathrm{m}}^n w_{\mathrm{m}}(r_i) p_{\mathrm{m}}^n(r_i) + \sum_{r_i} A_{\mathrm{cy}}^n w_{\mathrm{cy}}(r_i) p_{\mathrm{cy}}^n(r_i). \tag{10}$$

The weights were derived analytically from integration over the wedge geometry model. The expression for w_{m} was found by integration over the wedge surface, as well as the cell nucleus volume. The expression for w_{cy} was found by integration over the wedge volume and the cell nucleus.

4.3. Cross dose approximations

The wedge model can be computationally demanding for the cross dose contributions due to the large number of cells involved. The cross dose originates from neighboring cells at larger distance than a typical cell radius, and the exact cell shape is therefore expected to play only a minor role for the accuracy of the radiation intensity in a given cell nucleus. We therefore use a spherical approximation of the cells in the cross dose calculation to reduce the computational load. The cross dose due to irradiation of cell nucleus n is given by

$$\dot{D}^n(\text{cross dose}) = \sum_{k \neq n} A_{\mathrm{m}}^k S_{\mathrm{m}}(R_k^{eff}) + \sum_{k \neq n} A_{\mathrm{cy}}^k S_{\mathrm{cy}}(R_k^{eff}), \tag{11}$$

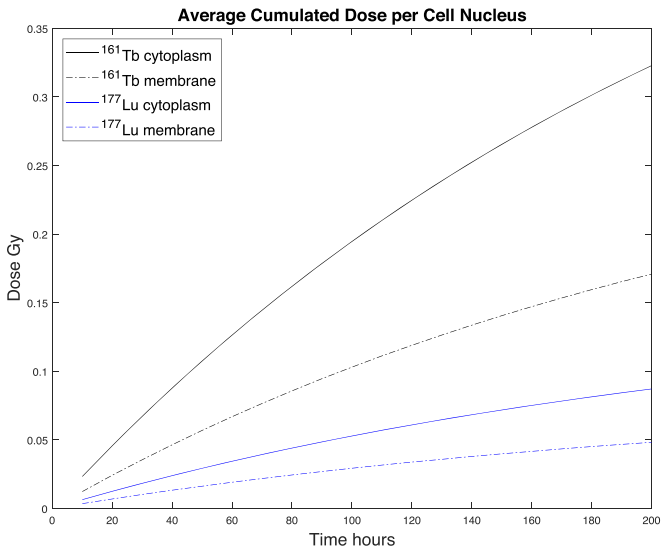

Figure 7. Average cumulated dose per cell for ^{177}Lu and ^{161}Tb with 100 kBq applied activity.

with an effective radius R_k^{eff} for the external cells k. The effective radius of these cells was based on the average measured area in the image plane. Rather than using images with a restricted number of cells for calculating the cross dose estimate, we assumed a homogeneous cell distribution and calculated the cross dose accordingly using the measured number density of cells in the images. This approach neglects the clustering of cells in the image plane. The cutoff radius in this calculation was based on the extension of the dose point kernels for a given nuclide.

5. Microdosimetric results

5.1. Comparison of the two nuclides

We used an internalization of PSMA-617 of 60% in the cytoplasm and 40% on the cell membrane. Liu *et al* (1998) The average cellular uptake of the applied activity was estimated to be in the range 1%–5%, and we assumed an uptake of 2%.

Figure 7 shows the calculated dose to the nucleus for 100 kBq of applied activity of ^{161}Tb and ^{177}Lu internalized to the cell surface and the cytoplasm. The low energy auger electrons emitted by ^{161}Tb have a short range, under 10 μm. This leads to a large increase in the dose to the nucleus in moving the ^{161}Tb from the cell membrane into the cytoplasm.

5.2. Cell viability experiments versus calculations

The cell survival probability P for each cell was evaluated using the LQ model, and a particular cell was marked 'alive' when a random trial number $\xi < P$, for $\xi \in [0, 1]$. The average survival probability N_{alive}/N was then calculated.

Figure 8 shows the survival curves as a function of applied activity for the cell experiments and the dosimetry calculations. The cell survival fraction is normalized by the number of cells in a control culture with no added activity. The computer model is normalized by the initial number of cells in the simulation.

Both the cell experiments and the dosimetry model show that ^{161}Tb is more effective than ^{177}Lu for the same applied activity. The cell experiments have an increase in cell viability over the control for values of applied activity under 50 kBq and the surviving fraction does not drop significantly below 95% until the applied activity is above 200 kBq. The computer model shows no such plateau since stimulation of cell growth at sub-lethal radiation doses is not accounted for in the model. Furthermore, the computer model does not account for cell division, and only estimates cell death based on the dose received in each cell nucleus.

The dosimetry model predicts a higher dose to the nucleus for ^{161}Tb than ^{177}Lu for the same applied activity due to the differences in radiation range. This is confirmed indirectly by the cell experiments, which show a lower cell survival fraction with ^{161}Tb than with ^{177}Lu. As such, the model is able to predict the relative effect from the two nuclides. The predicted cell survival rates are however influenced by the survival model used, and this is a nonlinear function of the accumulated dose.

As the auger electron density is significantly higher for ^{161}Tb, we may expect that two track bond breaking and the β parameter is in fact higher for ^{161}Tb than ^{177}Lu and the cell survival probability could be even lower

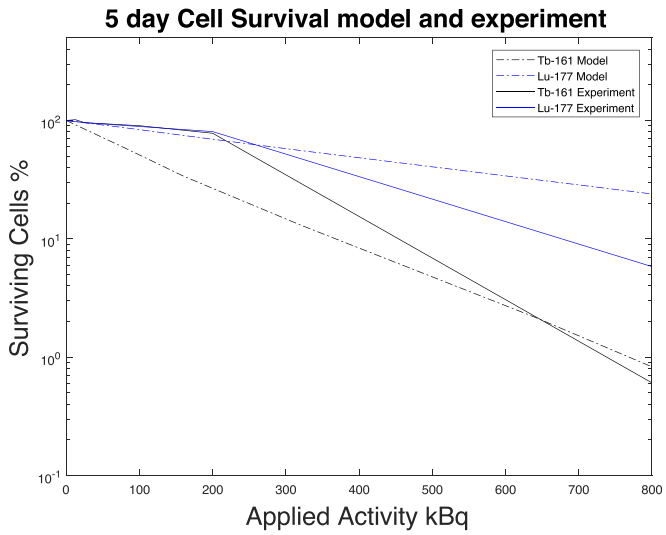

Figure 8. Survival curves after 5 d as a function of applied activity for ^{161}Tb and ^{177}Lu Cell experiments (solid lines) and dosimetry calculations (dash lines).

than what we have calculated. The beta-electron spectrum is similar between the nuclides and would only result in smaller variation in the α and β parameters. We can therefore infer that ^{161}Tb is a more efficient nuclide in terms of providing smaller cell survival probability, despite the uncertainty in the α and β parameters.

5.3. The effect of non-spherical and irregular cell geometries

The magnitude of the dose from the membrane to the nucleus increases with irregular cell models relative to spherical models. The radial PDF of a single irregular cell is wider (larger standard deviation) than for a spherical cell. The implication is that the smaller radii of the irregular cell provide a net increased dose from the cell membrane due to the nonlinear decay of the radiation intensity with distance, for the larger distances. The decrease in dose from the addition of larger radii is not sufficient to outweigh the effect of increased dose from the smaller radii. This effect is larger for shorter range auger electrons since the scale of variation of the dose point kernels are smaller, with larger effect from the nonlinearity of the dose-distance relationship. In conclusion, the actual non-spherical cell geometry has the effect of increasing the dose to the cell nucleus relative to the spherical model equivalent.

This effect was confirmed in a test case where an irregular cell using the wedge model for was compared to a spherical cell with the same volume. The dose to the nucleus from the cell membrane was calculated for both geometries. We found a significant deviation in the dose between the circular and the irregular cell of about 20%.

It is therefore important to account for the irregular cell geometry to obtain the correct dose magnitude. The change in dose magnitude (spherical versus irregular) depends on the radionuclide type. Thus, the relative change in dose (spherical versus irregular) between two different nuclides is likely to be different. The effect on the smaller cross dose contribution is likely to be less sensitive to the cell geometries due to the larger distances.

6. Discussion

Relative effect of different nuclides as function cell size and geometry. Auger electrons have a sufficiently short penetration length scale such that increasing cell size leads to a significant reduction of the dose to the cell nucleus from nuclides are situated on the cell membrane. The dose to the nucleus is then also highly sensitive to the cell geometry.

For a sufficiently large cells, conversion and beta-electrons may contribute more to the DNA-dose than auger electrons, and this would be the case irrespective of cell shape. The implication is that for the self dose for larger cells or for the cross dose, a specific auger emitter (here, terbium) may have less biological effect than a different nuclide with a larger fraction of beta and conversion electron energies (here, lutetium). The cross dose contribution is increased in a cell cluster as compared to a 'monolayer' of cells on a substrate. Thus, the longer range electrons will be more important in a tumor.

Radiation effects due to cell growth and cell death. We did not account for cell growth and cell splitting. The number of cells may also increase over time as an effect of low doses. In general, an account for cell splitting is potentially important since the radioactivity per cell is then reduced by a factor of two. This can accounted for in

the calculations by grouping the cells into separate populations or generations. However, this requires detailed history tracking of the cells. Dead cells still have radioactivity associated to them, they can provide a cross dose contribution to other cells. Hence, dead cells should be included in the calculations as well.

Radiation effects in cell clusters and tumors. For *in vivo* application one should include the kinetics of radionuclide transport into the tumor interior. Blood supply to the tumor interior both affects the cell viability and transport of radioactivity into the tumor volume. One would also expect diffusion of activity into the cell cluster via the intracellular volume between cell membranes. Thus both diffusion and advection effects will be important to consider in a complete microdosimetry approach. New *in vitro* experiments with 3D cell clusters are currently being set up by our group to shed light on the diffusion mechanisms and the effect of electron radiation on cell viability throughout the cluster.

Radiation effects from radionuclides on the cell membrane. The standard assumption in radioimmunotherapy has been that DNA bond breaking is the most important mechanism for disabling cancer cells. However, the effect of radiation from radionuclides located on the cell membrane has been under much debate recently. Radiation can affect the membrane directly by ionizing the membrane phospholipids locally near the receptor sites, or indirectly by ionization of water with subsequent oxidation effects (oxidative stress) (Paillas *et al* 2016). The latter mechanism seems to be more likely than poration of the membrane by direct ionization.

Non-internalized auger-emitting radionuclides prove, in some cases, to be more effective for cell death than radionuclides internalized into the cytoplasm (Pouget *et al* 2008). The central mechanism is that ionizing radiation initiates sphingomyelin hydrolysis to form ceramide (Haimovitz-Friedman *et al* 1994, Maier *et al* 2016, Paillas *et al* 2016) which can be sufficient to transduce apoptotic signals. Oxidation effects due to ionization of water near the cell membrane drives the catalysis of ceramide (Paillas *et al* 2016), and the cell membrane reorganizes following lipid raft formation.

The relative contribution to cell death by cell membrane radiation and irradiation of DNA in the cell nucleus should be explored further with microdosimetry. Since cell membrane irradiation is especially relevant for short range auger electrons in combination with moderate internalization fractions, it should be given more weight in upcoming microdosimetry research. However, the development of a mathematical/probabilistic models for the biological effect from cell membrane radiation must also also be developed to provide a complete model for the biological effect, or cell survival probability.

Improved cell survival probability models for microdosimetry. In the case for DNA irradiation, there is some uncertainty whether cell viability should be related to cumulated dose or other radiation quantities that better reflect the bond breaking probability (Bodgi *et al* 2016). For example, fluence or particle track density in the cell nucleus may correlate better to cell damage than the cumulated dose. The total dose can be achieved by either a few high energy particles or a larger number of small energy particles, and these are quite different physical scenarios in terms of ionization and molecular bond breaking. The probability of bond breaking and ionization in any molecule should be proportional to the local electronic track density provided that the particles have energies above the bond breaking (or ionization) energy threshold.

It has been debated whether the LQ model of dose-viability relations is oversimplified (McMahon 2018). In upgraded models one would simply attempt to replace these parameters with more direct physical radiation parameters such as track density and particle energy distribution that are readily available from Monte Carlo simulations. We will discuss these aspects further below.

A general strategy would be to correlate the measured cell viability to various physical quantities in the DNA volume that can be extracted from Monte Carlo simulations, such as track density, particle energy spectrum, and integrated dose. New probabilistic cell survival models that are better founded from a physical point of view can be developed from this approach.

Improved auger spectra. The contribution to the dose from the lower energy auger electrons is important over short distances, i.e. under 20 μm. We used decay spectra for the nuclides from the ENSDF database. These spectra may be inaccurate for the lower energy auger electron emissions and lead to errors in the calculated dose. These are calculated in the framework of the independent particle model underlying the Dirac–Hartree–Slater approach. However, this approach is only approximate for the outer shell transitions, and improved spectra may be computed using the multi-configuration Dirac–Fock method (MCDF). The MCDF calculation of the transition amplitudes show differences up to 20% and this may have an impact over small distances, on the order of micron (Sampaio 2019) between the emitter and the target. This is of relevance for calculated dose to the cell nucleus from internalized activity.

7. Conclusion

A microdosimetry model for auger-emitting radionuclides that incorporates *in vitro* cell geometries was developed and tested against measured cell survival probabilities. The microdosimetry calculations showed that

the accumulated dose in LNCaP prostate cancer cell nuclei from ^{161}Tb was higher than the dose from ^{177}Lu for the same applied activity. Both nuclides where conjugated to the same PSMA antibody. The reason for ^{161}Tb being a more efficient nuclide is that it has a higher number of short range auger electrons that contribute to the dose to the cell nucleus.

The β emission modes from both nuclides deposit energy in a larger volume than the auger electrons and will have a larger effect in close packed 3D cell clusters than in single layer cell experiments, where the cross dose between neighboring cells will be important. For the *in vitro* experiments we discussed, the cells were distributed on a plane and were less closely packed than in a tumor, and much of the energy from the beta is then deposited in the medium between cells and outside the cell-plane.

The effect of cell geometry (actual versus irregular as measured). The cell viability was estimated from the calculated accumulated dose in the cell nucleus volume, using the standard LQ model. The estimated values compared well with the experimental values, in the sense that the relative difference between the cell survival rates between the two nuclides were accurately predicted. As such, the current modeling approach can be used as a prediction tool for evaluating the variation of the biological effect from different radionuclides in a given cell and cell cluster geometry.

The absolute values of the predicted cell survival probabilities depend largely on the bias and uncertainties in the parameters of the LQ model, once the cell geometrical effects are accounted for. We foresee much improved survival models using α and β parameters that are modeled based on electron track density and energy spectra. These physical quantities are readily available from Monte Carlo simulations, and improved models for α and β would then provide better calibration of the predicted cell survival probabilities.

Acknowledgments

This research was funded by the Institute for Energy Technology through SIS strategic funding.

ORCID iDs

Teresa L Palmer https://orcid.org/0000-0001-7078-0784

References

Bodgi L, Canet A, Pujo-Menjouet L, Lesne A, Victor J-M and Foray N 2016 Mathematical models of radiation action on living cells: From the target theory to the modern approaches. A historical and critical review *J. Theor. Biol.* **394** 93–101

Cornelissen B and Vallis K 2010 Targeting the nucleus: an overview of auger-electron radionuclide therapy *Curr. Drug Discovery Technol.* **7** 263–79

Crouch S, Kozlowski R, Slater K and Fletcher J 1993 The use of atp bioluminescence as a measure of cell proliferation and cytotoxicity *J. Immunol. Methods* **160** 81–8

ENSDF: 2019 From ENSDF database as of 1 October, 2019, Evaluated and Compiled Nuclear Structure Data (bnl.gov)

Falzone N, Fernández-Varea J M, Flux G and Vallis K A 2015 Monte Carlo evaluation of auger electron-emitting theranostic radionuclides *J. Nucl. Med.* **56** 1441–6

Haimovitz-Friedman A, Kan C, Ehleiter D, Persaud R, McLoughlin M, Fuks Z and Kolesnick R 1994 Ionizing radiation acts on cellular membranes to generate ceramide and initiate apoptosis *J. Exp. Med.* **180** 525–35

Hanin L G and Zaider M 2010 Cell-survival probability at large doses: an alternative to the linear-quadratic model *Phys. Med. Biol.* **55** 4687–702

Hindie E, Zanotti-Fregonara P, Quinto M A, Morgat C and Champion C 2016 Dose deposits from ^{90}Y, ^{177}Lu, ^{111}In, and ^{161}Tb in micrometastases of various sizes: Implications for radiopharmaceutical therapy *J. Nucl. Med.* **57** 759–64

Lehenberger S, Barkhausen C, Cohrs S, Fischer E, Grünberg J, Hohn A, Köster U, Schibli R, Türler A and Zhernosekov K 2011 The low-energy beta and electron emitter ^{161}Tb as an alternative to ^{177}Lu for targeted radionuclide therapy *Nucl. Med. Biol.* **38** 917–24

Lindmo T and Bunn P 1986 Determination of the true immunoreactive fraction of monoclonal antibodies after radiolabeling *Methods Enzymol.* **121** 678–91

Liu H, Rajasekaran A K, Moy P, Xia Y, Kim S, Navarro V, Rahmati R and Bander N H 1998 Constitutive and antibody-induced internalization of prostate-specific membrane antigen *Cancer Res.* **58** 4055–60

Maier P, Hartmann L, Wenz F and Herskind C 2016 Cellular pathways in response to ionizing radiation and their targetability for tumor radiosensitization *Int. J. Mol. Sci.* **17** 102–34

Marcatili S, Pichard A, Courteau A, Ladjohounlou R, Navarro-Teulon I, Repetto-Llamazares A, Heyerdahl H, Dahle J, Pouget J P and Bardiès M 2016 Realistic multi-cellular dosimetry for ^{177}Lu-labelled antibodies: model and application *Phys. Med. Biol.* **61** 6935–52

Maria S D, Belchior A, Romanets Y, Paulo A and Vaz P 2018 Monte Carlo dose distribution calculation at nuclear level for auger-emitting radionuclide energies *Appl. Radiat. Isot.* **135** 72–7

McMahon S J 2018 The linear quadratic model: usage, interpretation and challenges *Phys. Med. Biol.* **64** 01TR01

Müller C, Reber J, Haller S, Dorrer H, Bernhardt P, Zhernosekov K, Türler A and Schibli R 2014 Direct *in vitro* and *in vivo* comparison of ^{161}Tb and ^{177}Lu using a tumour-targeting folate conjugate *Eur. J. Nucl. Med. Mol. Imaging* **41** 476–85

Oliver P A K and Thomson R M 2018 Investigating energy deposition within cell populations using Monte Carlo simulations *Phys. Med. Biol.* **63** 155018

Paillas S *et al* 2016 Localized irradiation of cell membrane by auger electrons is cytotoxic through oxidative stress-mediated nontargeted effects *Antioxidants Redox Signaling* **25** 467–84

Pedicini P, Strigari L and Benassi M 2013 Estimation of a self-consistent set of radiobiological parameters from hypofractionated versus standard radiation therapy of prostate cancer *Int. J. Radiat. Oncol. Biol. Phys.* **85** e231–7

Pouget J-P, Santoro L, Raymond L, Chouin N, Bardias M and Bascoul-Mollevi C 2008 Cell membrane is a more sensitive target than cytoplasm to dense ionization produced by auger electrons *Radiat. Res.* **170** 192–200

Sampaio J M 2019 Atomic physics inputs for enhanced targeted therapy *IBER 2019—Iberian Joint Meeting On Atomic and Molecular Physics* (https://doi.org/10.13140/RG.2.2.24932.53125)

Sefl M, Incerti S, Papamichael G and Emfietzoglou D 2015 Calculation of cellular s-values using geant4-dna: the effect of cell geometry *Appl. Radiat. Isot.* **104** 113–23

Steffen A-C, Göstring L, Tolmachev V, Palm S, Stenerlöw B and Carlsson J 2008 Differences in radiosensitivity between three her2 overexpressing cell lines *Eur. J. Nucl. Med. Mol. Imaging* **35** 1179–91

Valentin J 2003 Relative biological effectiveness (RBE), quality factor (Q), and radiation weighting factor (w_R): ICRP Publication 92 *Ann. ICRP* **33** 1–121

van Leeuwen C M, Oei A L, Crezee J, Bel A, Franken N A P, Stalpers L J A and Kok H P 2018 The alfa and beta of tumours: a review of parameters of the linear-quadratic model, derived from clinical radiotherapy studies *Radiat. Oncol.* **13** 96